CHEMISTRY OF MATERIALS

pubs.acs.org/cm

Article

Structural Evolution in Iron-Catalyzed Graphitization of Hard Carbons

Aurora Gomez-Martin, Zoe Schnepp, and Joaquin Ramirez-Rico*

Cite This: *Chem. Mater.* 2021, 33, 3087−3097

Read Online

ACCESS | Metrics & More | Article Recommendations | Supporting Information

ABSTRACT: Despite the recent interest in catalytic graphitization to obtain graphite-like materials from hard-carbon sources, many aspects of its mechanism are still poorly unknown. We performed a series of *in situ* experiments to study phase transformations during graphitization of a hard-carbon precursor using an iron catalyst at temperatures up to 1100 °C and *ex situ* total scattering experiments up to 2000 °C to study the structural evolution of the resulting graphitized carbon. Our results show that upon heating and cooling, iron undergoes a series of reductions to form hematite, magnetite, and wüstite before forming a carbide that later decomposes into metallic iron and additional graphite and that the graphitization fraction increases with increasing peak temperature. Structural development with temperature results in decreasing sheet curvature and increased stacking, along with a decrease in turbostratic disorder up to 1600 °C. Higher graphitization temperatures result in larger graphitic domains without further ordering of the graphene sheets. Our results have implications for the synthesis of novel biomass-derived carbon materials with enhanced crystallinity.

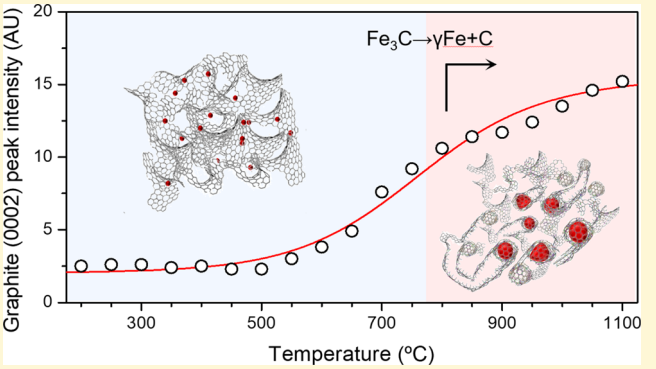

1. INTRODUCTION

An effective approach to accelerate the development of graphitic domains in non-graphitizing carbons at moderate temperatures (below 1600 °C) is the use of finely divided catalysts. This so-called *catalytic graphitization* involves the addition of foreign species to the carbon precursor that, upon heating, can induce the precipitation of ordered carbon regions and thus a decrease in the activation energy for crystallization.

The catalytic graphitization process received much attention in the 80s[1,2] due to the possibility of synthetizing graphite from hard carbons at temperatures far below what was conventionally required (3000 °C) by soft carbons, resulting in significant cost and energy savings. Similar approaches were later used extensively to grow carbon nanotubes (CNTs) by chemical vapor deposition (CVD).[3] However, despite the large body of work devoted to employing this method for the synthesis of carbon materials, the mechanisms of catalytic graphitization are still unclear and limited progress has been made in this direction. Currently, the attention is focused on the application of catalytically graphitized carbons in different advanced fields such as electrodes for supercapacitors,[4−6] anode materials for lithium-ion batteries,[7] and others[8,9] owing to their outstanding properties, including enhanced crystallinity[10] and electronic conductivity.[11]

Among the different catalysts employed, IV−VIII transition metals and especially Fe, Co, and Ni have stood out for their good graphitization efficiency. In this regard, of particular interest are previous studies from Maldonado-Hódar *et al.*,[12] Yan *et al.*,[13] Thambiliyagodage *et al.*,[14] and Sevilla *et al.*[15−17] evaluating the graphitization effectiveness of different transition metals with the same concentration on a certain carbon precursor. According to these studies, Fe shows the highest catalytic activity; however, transition metal oxides such as Fe_2O_3 and Fe_3O_4 and alloys such as Fe−Ni and Co−Ni have also proven to be effective catalysts.[18−20]

In graphitization, the peak heat treatment temperature is a key parameter.[10,21] From *in situ* XRD experiments from Hoekstra *et al.*,[22] the onset of the graphitization by Fe occurs from 715 °C, while Ni and Co require temperatures above 800 °C. From this temperature on, several authors have reported an increase in the degree of graphitization with increasing heat treatment temperature (HTT). Most studies are limited to low treatment temperatures and give no clear correlations between microstructural parameters and HTT,[23,24] but Ramirez-Rico *et al.*[25] reported an increase in the degree of crystallinity using Fe as a catalyst from 27 to 63% as treatment temperature

Received: November 16, 2020
Revised: April 15, 2021
Published: April 28, 2021

increases from 850 to 1600 °C, as calculated from Raman analysis. The increase in crystallinity was more pronounced in the 1100−1400 °C temperature range. A similar trend was also reported by Kakunuri *et al.*,[26] showing the largest extent of graphitization occurring between 900 and 1200 °C. So far, there is no clear evidence of a saturation point in the degree of crystallinity obtained from catalytic graphitization at a given catalyst loading.

Several mechanisms have been proposed for catalytic graphitization of carbon/iron mixtures, depending on the temperature range. At temperatures higher than the melting point of pure iron (∼1540 °C), graphite is known to form by a "*solution-precipitation*" mechanism, in which the molten iron becomes supersaturated with carbon that precipitates upon cooling as essentially defect-free graphite, as is the case with the graphite flakes that float on the liquid metal surface in blast furnace iron casting.[27] Since catalytic graphitization can take place at much lower temperatures, other mechanisms have been invoked,[28−30] involving the formation of highly supersaturated liquid droplets of Fe_xC_y.[31] According to this theory, droplets dissolve amorphous domains from the carbon matrix and precipitate as more ordered graphitic structures due to the associated reduction in free energy. Then, these droplets tunnel through the carbon matrix, as observed in *in situ* TEM experiments ([29] and the Supporting Information in ref 30), resulting in hollow graphitic tubes or channels.[15,28,32−35] Surprisingly, these droplets would form at temperatures much lower than the eutectic temperature of Fe−C (∼1150 °C) due to size effects and the structure of the amorphous carbon itself.[36] In many cases, X-ray diffraction of Fe-graphitized carbon samples reveals the presence of crystalline Fe_3C, whereas other authors report only the presence of metallic Fe (alpha-iron with a bcc structure) after cooling.

In this work, we carry out a series of experiments to shed light on the graphitization mechanism of hard carbon using Fe as a catalyst. First, we perform thermogravimetric (TGA)/differential scanning calorimetry (DSC) measurements of $FeCl_3$-impregnated biomass pyrolysis while simultaneously monitoring the composition of the released gases by mass spectrometry to precisely determine the onset temperature for graphitization. Then, we perform *in situ* synchrotron and laboratory X-ray diffraction experiments during pyrolysis to monitor the extent of graphitization and the evolution of the chemical state of the Fe catalyst. Finally, we perform total scattering experiments of carbon graphitized at different temperatures to determine the structural evolution of the resulting carbon material as a function of peak pyrolysis temperature by analyzing its pair distribution function.

2. EXPERIMENTAL SECTION

2.1. Sample Preparation. A commercial artificial medium density fiberboard (MDF) was chosen as a representative carbon precursor due to its low cost and homogeneity. As a route to homogeneously deposit fine iron particles into the resulting carbon, we chose to impregnate the biomass directly using an iron chloride solution that decomposes into iron upon heating. Iron-catalyzed graphitized carbon can thus be produced in a single high-temperature process: heating the impregnated precursor results in both the formation of a carbon scaffold and the decomposition of the catalyst precursor into metallic iron that then promotes carbon graphitization at higher temperatures.

In a typical synthesis process, cut and dried MDF wood pieces were impregnated with 1.0 M iron (III) chloride solution ($FeCl_3$, anhydrous 97% purity, *Panreac*) in isopropanol under vacuum for 2 h to ensure a homogenous impregnation. After impregnation, samples were then dried at 80 °C until complete solvent evaporation and constant weight are obtained. The mass gain was about 7 ± 2% with no external volume change.

Pyrolysis was carried out in a single-step process in a tube furnace under nitrogen flowing at 0.2 $L{\cdot}min^{-1}$. Impregnated samples were placed on alumina crucibles and then heated at a rate of 1 $°C{\cdot}min^{-1}$ up to 500 °C and then at 5 $°C{\cdot}min^{-1}$ up to the desired peak temperature (ranging from 850 to 1600 °C) followed by a holding time of 30 min and then cooled down at 10 $°C{\cdot}min^{-1}$ to room temperature. This temperature program was chosen to avoid cracks due to gas release during pyrolysis and to obtain defect-free monoliths. Samples pyrolyzed up to 2000 °C were also obtained in a two-step process: first carbonized up to 1000 °C as described above and then heated up to 2000 °C (5 $°C{\cdot}min^{-1}$, holding time 30 min) in a vacuum furnace (LHTG 200-300/30-2G—*Carbolite Gero GmbH & Co. KG*) under flowing argon. After pyrolysis, remaining Fe particles were removed by stirring in concentrated HNO_3 (69%, *Panreac*) followed by washing in deionized water until neutral pH.

2.2. Thermogravimetric Analysis Coupled with Mass Spectrometry. The thermal behavior of raw precursors during pyrolysis processes was characterized by thermogravimetric analysis (TGA) and differential scanning calorimetry (DSC) experiments, in which the weight and heat flow changes are measured *versus* a reference as a function of temperature. All measurements were carried out using a dual system (SDT Q-600, *TA Instruments*) between room temperature and 1000 °C at a heating rate of 10 $°C{\cdot}min^{-1}$ under a constant nitrogen flow rate of 100 $mL{\cdot}min^{-1}$. The instrument was coupled to a mass spectrometer (GSD 320 OmniStar, *Pfeiffer*) to evaluate the composition of evolved gases during pyrolysis. Mass/charge ratios between 10 and 50 u.m.a were considered, with a scan rate of 200 $ms{\cdot}(u.m.a)^{-1}$ and a secondary electron multiplier detector working at a voltage of 970 V.

2.3. *In Situ* X-ray Diffraction during Graphitization. The graphitization reaction was followed *in situ* using X-ray diffraction in the Material Science Powder Diffraction (MSPD) beamline of the ALBA-CELLS synchrotron (Cerdanyola del Vallés, Spain). Beam energy was 30 keV (wavelength λ = 0.4133 Å as confirmed using a Si standard) and scattering was measured up to $2\theta = 60°$ using an array of position-sensitive detectors (Dectris Mythen). Samples were contained in sealed quartz capillaries of 0.7 mm diameter. Since the release of volatiles during pyrolysis could break the containing capillaries, samples were prepared in a two-step process: MDF pieces were first carbonized to 1000 °C without any catalyst, as described in the previous section, and the obtained carbon pieces were then impregnated with 1 M $FeCl_3$ solution in isopropanol as explained before. This powder was then ground and sealed under vacuum in quartz capillaries for diffraction experiments. Diffraction patterns were obtained isothermally as a function of temperature in 50 °C increments from 300 to 800 °C and then back to 300 °C. The sample was heated using a hot-air blower, using a heating rate of 50 °C/min between isotherms.

Since the maximum temperature reached at the MSPD beamline was 800 °C, we carried out additional experiments at higher temperatures using a laboratory X-ray diffractometer equipped with a high-temperature reaction chamber (D8 Discover with a HIGH-temp furnace chamber, *Bruker*). The same sample was used in this case but under flowing nitrogen and at temperatures between 300 and 1100 °C. Additional details can be found in the Supporting Information.

2.4. Total Scattering Experiments. Total scattering experiments were performed at the MSPD beamline using the same conditions as described above. In this case, data were collected up to $2\theta = 120°$, resulting in a usable scattering vector range of $Q \sim 0.5{-}25$ $Å^{-1}$. The measurement time was 45 min per sample. Powdered graphitized carbon samples free of residual iron were contained in 0.7 mm polyimide tubes; an empty tube was also measured, and its background scattering signal was subtracted from the data. The pair distribution function (PDF) of each sample was calculated by Fourier transforming the coherently scattered signal using an *ad hoc*

https://doi.org/10.1021/acs.chemmater.0c04385
Chem. Mater. 2021, 33, 3087−3097

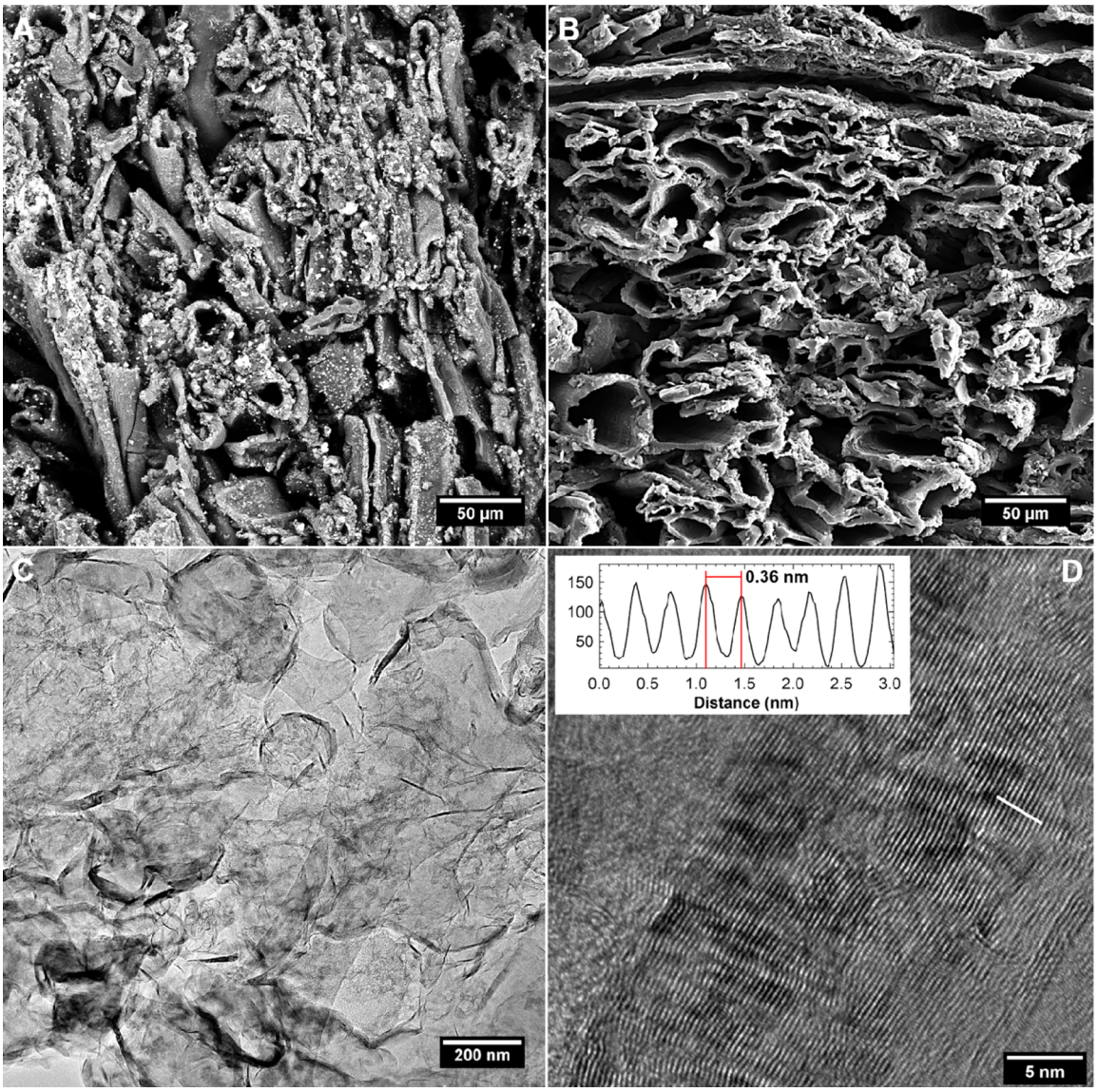

Figure 1. (A) Scanning electron micrograph of pyrolyzed, $FeCl_3$-impregnated medium density fiberboard. (B) Fe-catalyzed carbon derived from MDF-pyrolysis, after removal of Fe particles. (C) Transmission electron micrograph of Fe-graphitized carbon processed at 1600 °C and (D) high-resolution TEM micrograph showing detailed (002) lattice fringes of ordered graphitic regions.

polynomial correction as implemented in PDFGetX3 software.[37] Further analysis of the obtained PDFs was performed using PDFGui.[38]

3. RESULTS AND DISCUSSION

3.1. Electron Microscopy. The microstructure of Fe-graphitized carbon from the pyrolysis of the MDF is shown in Figure 1. The structure of the original wood precursor, made of hollow, pressed cellulose fibers, is maintained after graphitization. The obtained carbon material is decorated with Fe nanoparticles (panel A) that are removed after etching with concentrated HNO_3 (panel B). The weight content of Fe within the carbon was ∼11% after graphitization and below 0.5% after acid etching, as measured using ICP-OES. Under a transmission electron microscope (panel C), flat ordered regions are observed and so are hollow carbon spheres, as has been reported previously for this material.[21] The high-resolution micrograph of panel D confirms the appearance of a graphitic structure. A line profile across stacked graphene layers allows us to estimate the interplanar distance between layers as (0.36 ± 0.01) nm, slightly larger than the theoretical interplanar spacing of graphite (0.336 nm, ICDD card 41-1487).

3.2. TGA and Mass Spectroscopy Analysis. Thermogravimetric and differential scanning calorimetry analyses coupled with mass spectrometry were carried out to study the thermal behavior of catalyzed/non-catalyzed MDF samples and evolved gases while heating under flowing nitrogen. Furthermore, $FeCl_3$ powders were also characterized for comparison purposes. Figure 2 shows TGA and DSC analysis under an inert atmosphere of the raw MDF precursor without a catalyst (a), $FeCl_3$ powder (c), and MDF impregnated with 1.0 M $FeCl_3$ solution (e). Right panels in Figure 2 (b,d,f) show associated mass spectrometry representation (treatment temperature *vs* mass/charge ratio) where the signal intensity is represented in log units, indicating the evolution of gas products during thermal decomposition. A constant background signal on the mass spectrum due to nitrogen (m/z = 14, 28, 29 a.m.u), water vapor (m/z = 18 a.m.u), oxygen (m/z

https://doi.org/10.1021/acs.chemmater.0c04385
Chem. Mater. 2021, 33, 3087−3097

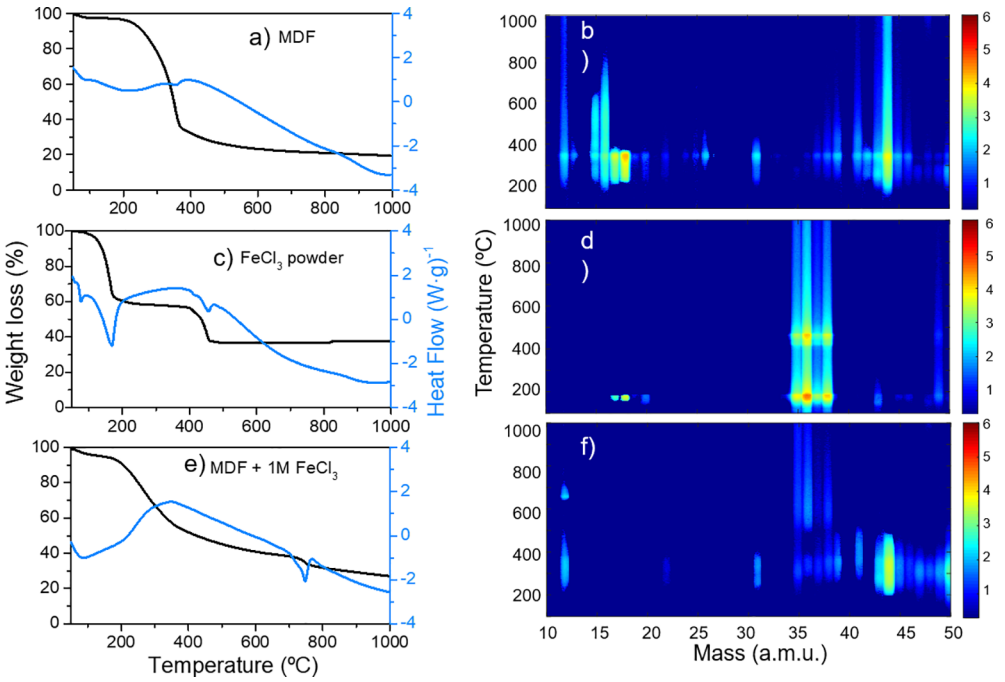

Figure 2. TGA and DSC analysis along with mass spectrum of evolved gases (treatment temperature *vs* mass/charge ratio) of a raw MDF (a,b), $FeCl_3$ powder (c,d), and MDF impregnated with 1.0 M $FeCl_3$ solution (e,f) heating at 10 °C·min^{-1} under an inert atmosphere. Normalized mass spectra are represented as a function of pyrolysis temperature for different mass values in terms of the logarithm of the ion current in arbitrary units.

= 16, 32 a.m.u), and carbon dioxide (m/z = 44 a.m.u) from the vacuum chamber and sealing was subtracted from the data.

The raw MDF precursor (Figure 2a,b) exhibits two main weight loss stages in the TGA curve. The first one, which takes place at temperatures below 200 °C, corresponds to the water desorption, while the second stage between 250 and 500 °C is due to the thermal decomposition of polysaccharide chains and breakdown of C−O, C−C, and C−H bonds, leaving a solid carbon template of about 20−25% of the original weight precursor at temperatures above 600−700 °C. Most evolved gases are released in the same temperature range, between 200 and 500 °C. The main evolved gases upon pyrolysis are[a] CO_2 (m/z = 12, 22, 44 a.m.u), CO (m/z = 12, 14, 28), O_2 (m/z = 16, 32 a.m.u), and H_2O (m/z = 16, 17, 18, 32 a.m.u) and signals from hydrocarbons such as CH_4, C_2H_4, and C_2H_6 (at m/z = 12−16, 24−27, 38−44 a.m.u).[39] From the DSC curves (blue color), the pyrolysis process is mainly endothermic, as energy is required to break the polysaccharide chains.

$FeCl_3$ powder (Figure 2c,d) decomposes in two stages until reaching 460 °C.[40] These two stages are attributed to the loss of chlorine (as confirmed by the mass spectrum and the increased ion current at m/z = 35−38 a.m.u) due to the decomposition of $FeCl_3$, leaving behind a 35 wt % of remaining Fe. At 150 °C, the release of adsorbed water (m/z = 16−18 a.m.u) is also observed. Reference work indicates that hydrated $FeCl_3$ decomposes in the 200−500 °C range to produce iron oxide or hydroxide species[41−43] due to the decomposition of (1) $FeCl_3 \rightleftarrows FeCl_2 + 1/2Cl_2$ (∼200 °C) and then (2) $FeCl_2 \rightleftarrows Fe + Cl_2$ (460 °C), leaving behind 35 wt % of remaining Fe, similar to our observations. It is therefore reasonable to assume that the loss of chlorine indicates decomposition of the $FeCl_3$ precursor to produce the catalyst precursor nanoparticles in our system.

The MDF impregnated with 1.0 M $FeCl_3$ solution (Figure 2e,f) exhibits a similar behavior during pyrolysis to that of the raw MDF but shows a narrower main weight loss of the cellulosic-based precursor at temperatures ranging between 200 and 500 °C, as seen in the mass spectra. The thermal decomposition of the catalytic agent is detected by the release of chlorine (m/z = 35−38 a.m.u; Figures 2f and 3a) that occurs over a wider temperature range (with peak rates at 337 and 600 °C) when compared to $FeCl_3$ powder (with maximum rate decomposition at 177 and 462 °C; Figure 3b) upon heat treatment. At 700−750 °C, we observe an additional weight loss and an endothermic peak on the heat flow curve, which can be attributed to the carbothermic reduction of iron oxide and subsequent formation of iron carbide (Figure 2e). This can be correlated with the release of CO_2 species (m/z = 44 a.m.u; Figures 2f and 3c) that does not occur on the raw MDF without a catalyst (Figure 3d).

3.3. *In Situ* XRD Experiments. Figure 4a shows scattered intensity from synchrotron X-ray diffraction experiments as a function of the temperature and diffraction angle recorded *in situ* during heating of a carbon sample impregnated with $FeCl_3$ up to 800 °C, whereas Figure 4b shows selected diffraction patterns at specific temperatures with marks corresponding to the main observed reflections. At 300 °C, a shoulder or bump at 2θ ∼6° (λ = 0.4134 Å) related to amorphous carbon areas can be observed, along with diffraction reflections of hematite (Fe_2O_3—ICDD card 39-1346), which is consistent with the thermal decomposition of $FeCl_3$ in air at this temperature.[44] Fe_2O_3 reflections are observed upon heating up to 400 °C, at which point it transforms into magnetite (Fe_3O_4; ICDD card 76-0955). A further increase in the treatment temperature up to 700 °C subsequently transforms Fe_3O_4 into wüstite (FeO; ICDD card 03-0968), which finally undergoes carbothermic reduction to form an intermediate carbide, cementite (Fe_3C; ICDD card 35-0772). At 750 °C, the apparition of a broad asymmetric peak at 2θ ∼7° indicates the presence of graphite−(002) reflection and thus the onset of graphitization. This

https://doi.org/10.1021/acs.chemmater.0c04385
Chem. Mater. 2021, 33, 3087−3097

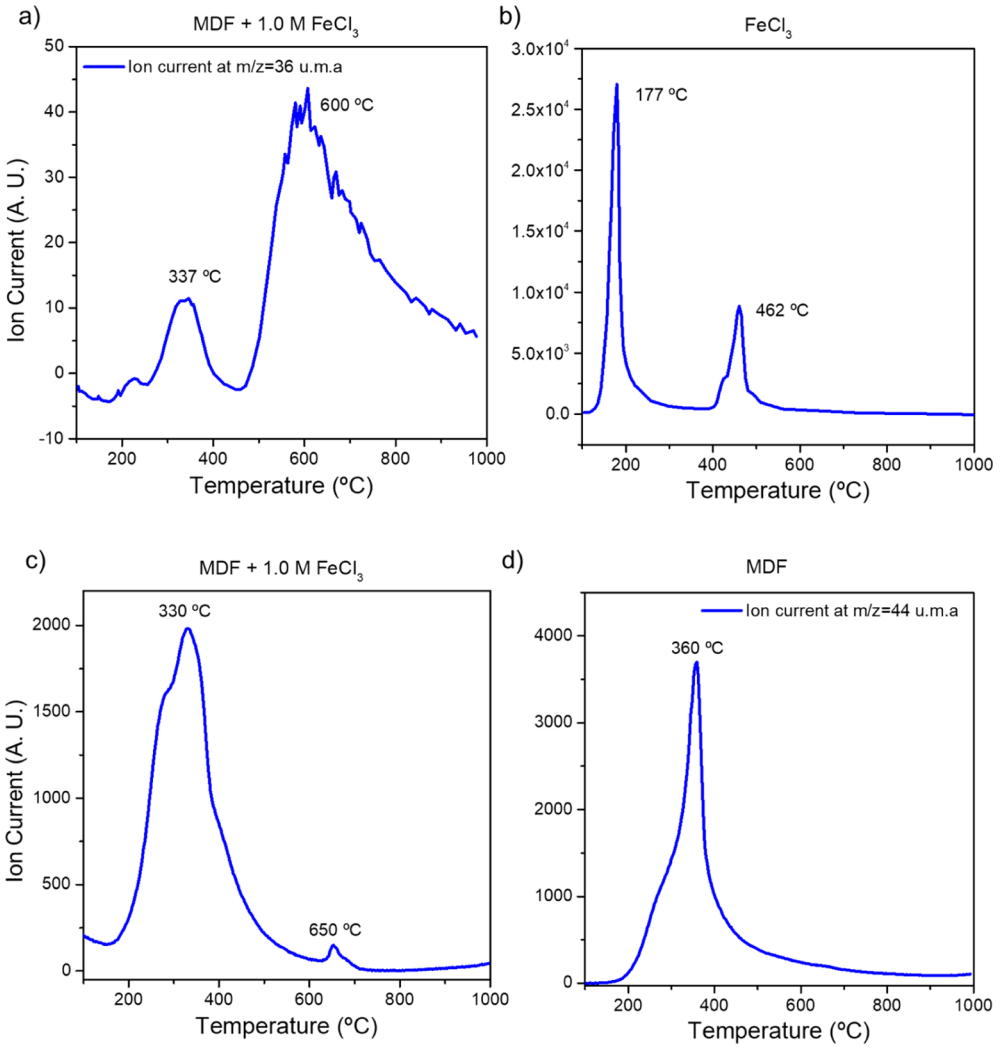

Figure 3. Mass spectra. Top panels: ion current signal *vs* treatment temperature at m/z = 36 u.m.a related to evolved Cl_2 gases for (a) MDF impregnated with 1.0 M $FeCl_3$ and (b) $FeCl_3$ powder. Bottom panels: ion current signal *vs* treatment temperature at m/z = 44 u.m.a related to evolved CO_2 gases for (c) MDF impregnated with 1.0 M $FeCl_3$ and (d) MDF without Fe.

phase reflects the uptake of carbon into iron oxide nanoparticles and reaches its maximum intensity at 800 °C. At 800 °C, Fe_3C and fcc iron phases (γ-Fe; ICDD card 52-0512) coexist. As the sample is cooled down, the Fe_3C phase decomposes into γ-Fe, which then transforms at 700 °C (close to the theoretical transformation temperature, 727 °C) into ferrite (α-Fe; ICDD card 06-0696).[45] After cooling down to room temperature, the only large reflections apart from those of graphite correspond to α-Fe. More details about the phase composition as a function of temperature as determined from Rietveld refinement can be found in the Supporting Information (Figures S1−S5).

To reach higher temperatures, we used a laboratory diffractometer equipped with a high-temperature chamber and carried out experiments between 300 and 1100 °C. Most important results are shown in Figure 5 (full results in the Supporting Information). At 750 °C, a mixture of Fe_3C and metallic γ-Fe (fcc) is observed, in agreement with synchrotron XRD data. Upon further heating, the carbide decomposes and only metallic γ-Fe is observed, apart from some small peaks due to the alumina sample holder (Figure 5a). The intensity of the (002) reflection of graphite monotonically increases with the temperature up to 1100 °C (Figure 5b), even though cementite decomposition starts at ∼800 °C.

3.4. Total Scattering Experiments and Pair Distribution Function Analysis. Diffraction measurements up to $Q \sim 0.5-25$ Å^{-1} were performed on carbon samples graphitized at temperatures from 850 to 2000 °C, after the removal of Fe, as described in the material section. Figure 6 shows the normalized scattering factors (related to the diffracted intensity) as a function of Q, zooming into the 1.6−2.2 Å^{-1} region (panel a), where the (002) peak from graphite is located. A qualitative assessment of these data reveals an increased crystallinity with increasing graphitization temperature, as evidenced by the sharpening of the diffraction peaks. Fourier transforming these data allowed us to calculate and further analyze the pair distribution function (PDF) to extract information on the degree of structural development of biomass-derived carbon upon graphitization using the Fe catalyst.

The PDF is a very powerful tool for the study of materials that show limited crystallinity and only local ordering,[46] especially for carbon materials. One of the earliest examples is from R. Franklin,[47,48] who studied the structural differences between graphitizable and non-graphitizable carbon from

https://doi.org/10.1021/acs.chemmater.0c04385
Chem. Mater. 2021, 33, 3087−3097

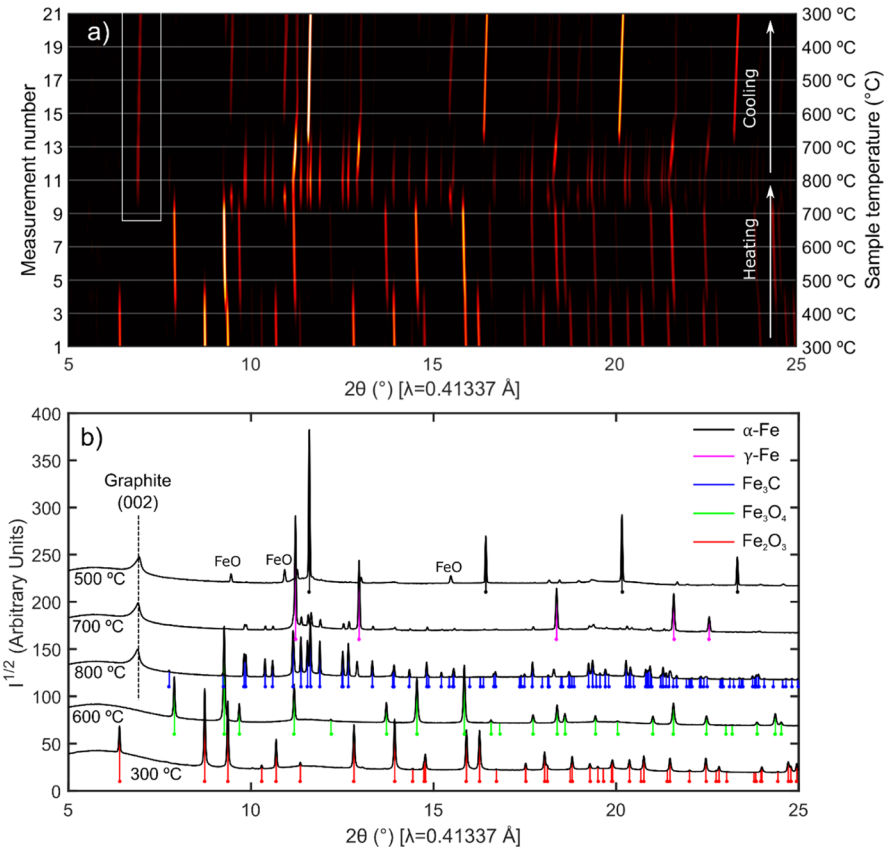

Figure 4. Graphitization measured *in situ* using synchrotron X-ray diffraction. (A) Two-dimensional plot showing diffracted intensity as a function of temperature and scattering angle 2θ. In this experiment, the temperature first rises from 300 to 800 °C (measurements 1−11) and then decreases back to 300 °C (measurements 12−21). The (002) reflection from graphite is marked with a white line. (B) Line plots of diffracted intensity as a function of angle 2θ for selected temperatures, along with the position of reflections of the crystalline phases identified at each temperature. The formation of graphitic regions results in the appearance of an asymmetric peak at a position close to the (002) reflection of graphite (marked with a dashed line).

different polymeric precursors. Several applications of the PDF to the study of carbon obtained by pyrolysis[49,50] and other turbostratic layered materials can be found in the literature.[51]

The PDF contains information regarding the interatomic distances in a solid, irrespectively of its crystalline or amorphous character. For X-rays, it is defined as

$$G(r) = \frac{1}{r}\sum_{ij}\frac{b_i b_j}{b^2}\delta(r - r_{ij}) - 4\pi\rho_0 \tag{1}$$

where r_{ij} represents the interatomic distance between atoms i and j and b_i is the scattering length of atom i and ρ_0 is the average atomic density. It can be computed from the scattered intensity $S(Q)$ of a powdered (isotropic) material by means of the following relationship

$$G(r) = \frac{2}{\pi}\int_0^\infty Q[S(Q) - 1]\sin(Qr)\mathrm{d}Q \approx \frac{2}{\pi}\int_{Q_{min}}^{Q_{max}} Q[S(Q) - 1]\sin(Qr)\mathrm{d}Q \tag{2}$$

with Q being the modulus of the scattering vector. Since the available Q-range is limited in any diffractometer, the obtained function approximates the real one due to truncation effects. In the PDF, each atomic pair distance manifests as a peak that is centered on the average distance and has a finite width since interatomic distances may vary due to at least atomic thermal motion. For very crystalline materials, the PDF oscillates around zero and exhibits peaks up to very large interatomic distances (>100 Å), its range being limited only by the diffractometer angular resolution. In nanomaterials or materials with limited long-range ordering, the amplitude of the PDF decays with increasing interatomic distances, and this decay allows for estimation of the crystalline domain or crystallite size.

Further insight into the atomic ordering from the analysis of PDFs requires a structural model that can be fitted to the observed data, from which structural parameters can be refined. Although several approaches exist, we have performed the so-called *small-box* modeling using the crystalline structure of graphite as a starting point. This approach has been successfully employed in the past to study hard carbons and starts by postulating a crystalline structure that contains the basic short-range atomic unit (hexagonal carbon rings in this case) and smoothing out the long-range correlations by introducing *long-range* disorder. We introduce this disorder through anisotropic *atomic displacement parameters* (ADPs), which are allowed to take unphysical values describing *static* disorder, as opposed to thermal motion.[49] In our analysis, we refined the lattice parameters a and c and anisotropic displacement parameters U_{ii} and an average crystallite size and a global scale factor.[52] To maintain consistency with the in-plane symmetry of the graphene layers, we fixed $U_{22} = U_{11}$

https://doi.org/10.1021/acs.chemmater.0c04385
Chem. Mater. 2021, 33, 3087−3097

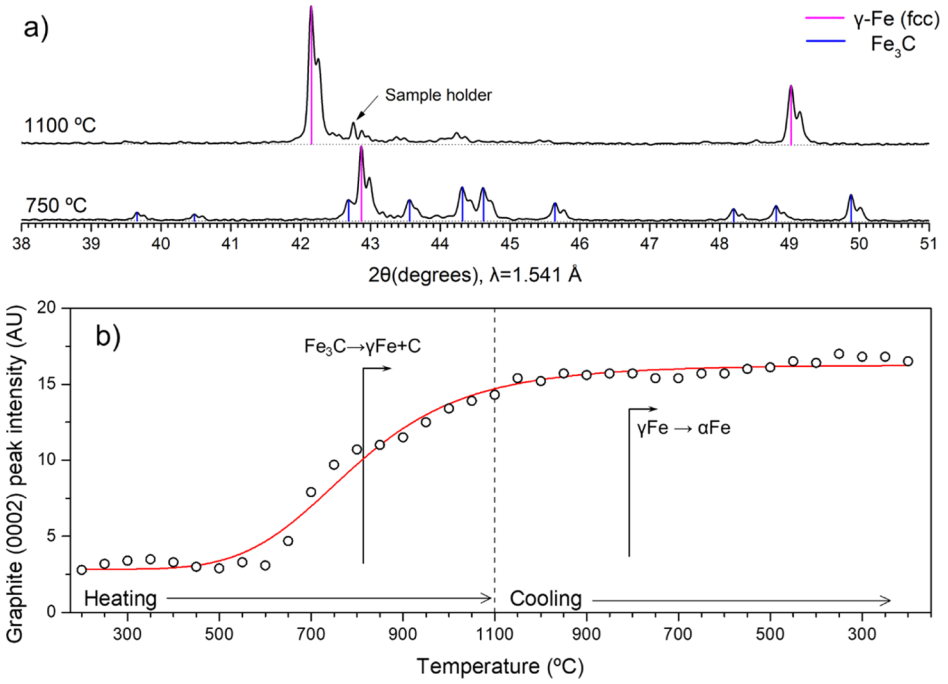

Figure 5. (a) High-temperature diffraction experiments in a laboratory diffractometer. The bottom diffraction pattern was obtained at 750 °C and shows reflections from both Fe_3C and metallic γ-Fe. Upon further heating, the carbide decomposes, leaving only metallic γ-Fe at 1100 °C (upper diffraction pattern). (b) Evolution of the (002) reflection intensity of graphite as a function of temperature (laboratory diffractometer). The temperatures at which the cementite decomposition and the fcc-to-bcc transformation of iron are observed are marked. The red line is only included as a visual aid and does not imply any particular model to fit the data.

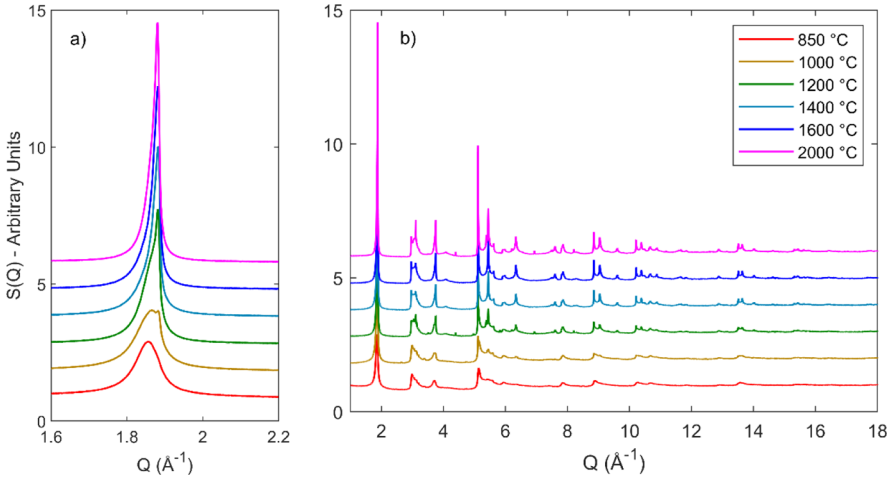

Figure 6. Normalized scattering factor for the Fe-graphitized MDF at different carbonization temperatures. Panel A shows a magnified view of the region containing the reflection from the (002) planes in graphite.

and U_{12} = 1/2 U_{11} and independently refined U_{11} and U_{33} to probe both in-plane and out-of-plane disorder in the structure.

The observed PDFs along with the fitting to the calculated PDFs from the refined structural model and the difference between the two are shown in Figure 7a,b for carbons obtained at 850 and 2000 °C. In all cases, the number of fitting parameters was restricted to six (a, c, U_{11}, U_{33}, crystallite size, and a global scale factor) and refinement was performed in the range 0.5−20 Å for r. Agreement factors R_w were generally below 20%[b]. While this number might appear high when compared to typical R_{wp} values attainable in Rietveld refinements, goodness-of-fit metrics cannot be directly compared between the two methods, and R_ws greater than 15% are common in real-space refinements of well-crystallized materials.[51] In general, a good correspondence between measured data and the model PDF could be obtained, as can be seen from the fits. The parameters from the refinements are shown as a function of graphitization temperature in Figure 7c−f.

Evolution of the calculated lattice parameters of the average disordered structure evidence a progressive enhancement of crystallinity with increasing graphitization temperature. By looking at the parameter a (Figure 7c), which is related to the average *in-plane* interatomic distances in the structural graphene unit, we see that at temperatures in the range 850−1200 °C, calculated lattice parameters are lower than those of ideal graphite (a = 2.461 Å, marked with a dashed horizontal line in panel c), which is indicative of sheet

https://doi.org/10.1021/acs.chemmater.0c04385
Chem. Mater. 2021, 33, 3087−3097

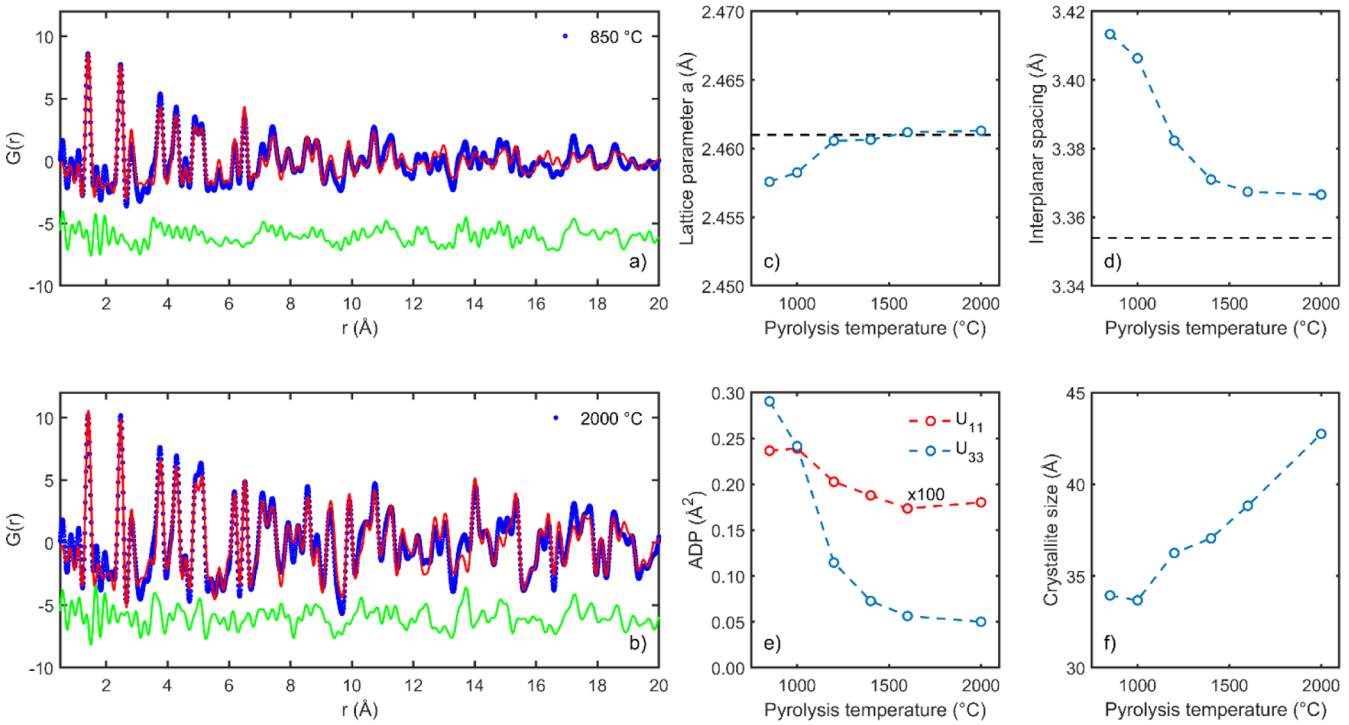

Figure 7. (a,b) Observed PDF (blue circles), fitted profile (red line), and difference (green line) for graphitized carbon at 850 °C (panel a) and 2000 °C (panel b). (c,d) Lattice parameter *a* and interplanar spacing ($c/2$) obtained from fitting the observed PDFs to a disordered graphite structure, as a function of temperature. Dashed black lines show the theoretical values for graphite. (e) In-plane (U_{11}) and out-of-plane (U_{33}) atomic displacement parameters from the fit as a function of temperature. Note that U_{11} is multiplied by a factor of 100. (f) Crystallite size as a function of temperature.

curvature in the stacked graphene layers.[53] However, the value of the lattice parameters progressively increases and reaches the theoretical value at a pyrolysis temperature of 1400 °C and remains virtually constant thereon, suggesting that increasing pyrolysis temperature decreases sheet curvature as graphene layers become planar and stacked on top of each other. The importance of the peak pyrolysis temperature can also be seen in the evolution of the interlayer or interplanar spacing between graphene sheets (theoretical value for graphite is $1/2c$ = 3.354 Å, again marked with a dashed line) shown in Figure 7d. The interplanar spacing progressively decreases with increasing pyrolysis temperature until reaching a constant value of 3.36 Å for temperatures above 1400 °C.

Further evidence on this increased ordering is observed in the evolution of ADPs with increasing graphitization temperatures. The values of U_{11} (Figure 7e), related to *in-plane* disorder, progressively decrease up to 1400 °C and thereon become constant, reaching 1.8 × 10^{-3} Å^2, a value that is physically compatible with thermal motion. Similarly, the values of U_{33} decrease with the temperature up to 1600 °C as well due to the rapprochement between graphene layers and reach about 0.05 Å^2, a value that is 2 orders of magnitude larger than U_{11} and can be interpreted in terms of turbostratic disorder.

3.5. Graphitization Mechanism. It is then clear from the results that the extent of graphitization in hard carbon using Fe as a catalyst is mainly determined by the peak reaction temperature. Previous studies showed this dependence using other techniques such as Raman spectroscopy and the corresponding decreased intensity ratio between D_1 and G bands when increasing the pyrolysis temperature.[7,21] Several authors attribute the graphitization to the initial formation of an iron carbide phase that continuously forms and decomposes into ordered graphitic carbon. According to these studies, the formation of Fe_3C is responsible for graphitization, and the fact that only metallic Fe is observed on samples graphitized at temperatures above 1000 °C is explained by decomposition of the carbide into Fe and C upon cooling.[29,31] Our *in situ* observations partially support this theory but also give additional insight into the process, which can be summarized as follows:

1 At temperatures below ∼700 °C, Fe resulting from the thermal decomposition of $FeCl_3$ goes through several oxidation states as it is progressively reduced from Fe_2O_3 to Fe_3O_4 and finally to FeO at ∼700 °C. Both the structure of the biomass precursor and the nature of the initial Fe source and concentration would play a key role in the graphitization process. Previous studies showed that impregnation of lignocellulosic biomass with $FeCl_3$ results in degradation of hemicellulose and selective hydrolysis of cellulose.[54−56] This would explain the different thermal evolution and release of CO_2 and Cl_2 species upon pyrolysis of $FeCl_3$-impregnared biomass in comparison to the decomposition of raw biomass and $FeCl_3$ separately (Figure 3).
2 Then, at ∼700 °C, FeO is fully reduced into metallic Fe as observed by both X-ray diffraction and TGA/DSC/mass spectroscopy experiments. This endothermic process is observed in the DSC, and the carbothermic reduction is evidenced by the release of CO_2 species at such a temperature range. Immediately, Fe_3C is formed and graphitization starts, resulting in the presence of a peak close to the (002) interplanar spacing of graphite in the X-ray diffraction pattern.

https://doi.org/10.1021/acs.chemmater.0c04385
Chem. Mater. 2021, 33, 3087−3097

3 At temperatures above 750 °C, the carbide phase (Fe_3C) partially decomposes into metallic Fe with a fcc structure (austenite, γ-Fe), which is the equilibrium phase of metallic iron at temperatures higher than ∼727 °C. Although the formation/decomposition of a carbide phase would play a key role in the graphitization at temperatures <800 °C upon heating, our insitu experiments suggest that the absence of Fe_3C reflections at temperatures above 800 °C indicates that this mechanism would not be dominant at high temperatures. Nevertheless, the Fe_3C decomposition into Fe with a bcc structure (ferrite, α-Fe) and C upon cooling gives for the first time clear evidence of the formation of additional graphitic regions, which may be explained by the decreased solubility of carbon into the metal catalyst particles with decreasing temperature and the precipitation of ordered carbon surrounding the catalyst particle core to reduce the surface energy upon cooling.[57−59]

4 Our PDF results indicate that structural evolution continues from 800 °C and up to 2000 °C, not only increasing the average size of the graphitic domains but also resulting in flattening and stacking of graphene sheets. The largest degree of structural development occurs in the 1000−1600 °C range, as determined from the analysis of pair distribution functions of the resulting graphitized carbon. The decreased sheet curvature and increased stacking level of graphene sheets with lower turbostratic disorder at temperatures >1400 °C would be attributed to the precipitation of three-dimensional graphite crystals due to a higher catalyst particle size. Previous studies on catalytic graphitization using Ni as a catalyst[35,60] have been invoked by transmission microscopy analysis that at lower temperatures, the graphitization takes place by deposition of curved graphene layers surrounding Ni particles of a few nanometers in size, while at higher temperatures (>1400 °C), the coarsening of catalyst droplets promotes the formation of three-dimensional graphite platelets by a solution precipitation mechanism. The abrupt decrease in interplanar distances and U_{33} values would be related to the precipitation of less-defective graphite crystals, in comparison to lower temperatures where the carbon exhibits a higher curvature and turbostratic disorder.

Clearly, graphitization by transition metal catalysts is a complex phenomenon that can proceed by several, concurrent routes depending on the chemical state and the size of the catalyst particles. A simple calculation performed using FactSage[61] yields the following Gibbs' free energies at T = 765 °C (normalized per mol Fe)

$$6FeO + 5C \rightarrow 6Fe + 2C + 3CO_2, \quad \Delta G = -0.60\ \text{kJ/mol} \tag{3}$$

$$6Fe + 2C \rightarrow 2Fe_3C, \quad \Delta G = +0.30\ \text{kJ/mol} \tag{4}$$

Therefore, the early formation of Fe_3C is thermodynamically favored when FeO is carbothermically reduced, whereas the formation of Fe_3C directly from metallic Fe (reaction 4) will only occur spontaneously at temperatures over ∼820 °C. This is in agreement with the *in situ* observations of Hoekstra *et al.*[22] who reported the onset of graphitization in the Fe−C system and formation of Fe_3C at temperatures as low as 715 °C. The formation of the carbide might also explain why Fe is a more effective bulk graphitization catalyst than Ni or Co, as there is no stable carbide phase in the Ni−C and Co−C phase diagrams.[62]

The nanosized nature of the catalyst particles resulting from the decomposition of the $FeCl_3$ precursor probably explains why graphitization occurs at much lower temperatures in our system than that observed by Li *et al.*[63] (∼1200 °C), who mixed powders of milled coke carbon and iron (particle sizes <74 and <5 μm, respectively). The large particle sizes of Fe in the cited study probably limited the formation of Fe_3C due to the sluggish diffusion kinetics, and thus, graphitization only started when a liquid phase formed *via* a solution reprecipitation mechanism. Due to the large size of the particles, this liquid phase formed at temperatures above the Fe−C eutectic (∼1150 °C), whereas in our system, it occurs much earlier due to the nanosized nature of the Fe particles.

4. CONCLUSIONS

Iron is an effective catalyst for the graphitization of hard carbons obtained from the pyrolysis. Understanding the graphitization mechanism by transition metals is of utmost importance for the future design of graphitic materials. A series of *in situ* experiments were herein carried out using Fe to shed light on the graphitization mechanism of a hard carbon. A homogeneous distribution of fine nanosized Fe particles within the carbon precursor was obtained after impregnation with $FeCl_3$. The temperature at which graphitization takes place is influenced by the local structure of the amorphous carbon and the size and initial oxidation state of the catalyst. Our results show that when deposited *in situ*, decomposition of the Fe precursor proceeds by a series of reductions, from Fe_2O_3 to FeO and finally to Fe, which favors the early formation of Fe_3C, promoting the graphitization of hard carbon at temperatures as low as 750 °C. However, Fe_3C reflections are absent at temperatures over 800 °C, indicating that the formation/decomposition of Fe_3C is not responsible for graphitization at higher temperatures. The largest structural development occurs in the 1000 °C−1600 °C temperature range. A monotonically increase in long-range ordering and decreased sheet curvature of the resulting graphitic carbon are observed at temperatures up to 1600 °C. At higher temperatures, the graphitic domains grow without an increase in local ordering: both the interplanar spacing between the graphene sheets and the turbostratic disorder remain constant up to 2000 °C.

■ ASSOCIATED CONTENT

Supporting Information

The Supporting Information is available free of charge at https://pubs.acs.org/doi/10.1021/acs.chemmater.0c04385.

Results of Rietveld refinement of *in situ* synchrotron data and results of *in situ* diffraction experiments on a laboratory diffractometer upon heating from 200 to 1100 °C and cooling back to 200 °C (PDF)

■ AUTHOR INFORMATION

Corresponding Author

Joaquin Ramirez-Rico − *Departamento Fisica de la Materia Condensada and Instituto de Ciencia de Materiales de Sevilla, Universidad de Sevilla—CSIC, Sevilla 41012, Spain;* orcid.org/0000-0002-1184-0756; Phone: +34 954550963; Email: jrr@us.es

https://doi.org/10.1021/acs.chemmater.0c04385
Chem. Mater. 2021, 33, 3087−3097

Authors

Aurora Gomez-Martin − *Departamento Fisica de la Materia Condensada and Instituto de Ciencia de Materiales de Sevilla, Universidad de Sevilla—CSIC, Sevilla 41012, Spain;* orcid.org/0000-0001-7053-3986

Zoe Schnepp − *School of Chemistry, University of Birmingham, Birmingham B152TT, U. K.*

Complete contact information is available at: https://pubs.acs.org/10.1021/acs.chemmater.0c04385

Notes

The authors declare no competing financial interest.

■ ACKNOWLEDGMENTS

The authors from the University of Seville acknowledge funding by the Spanish Government Agency *Ministerio de Ciencia, Innovación y Universidades* under grant PID2019-107019R. *In situ* synchrotron x-ray diffraction and total scattering experiments were performed at the MSPD beamline at ALBA Synchrotron with the collaboration of ALBA staff. SEM, TEM, and TGA/DSC coupled with mass spectrometry and laboratory X-ray diffraction experiments were performed at the CITIUS central services of the University of Seville (Spain).

■ ADDITIONAL NOTES

[a]Mass (u.m.a): 12 (C^+ from CO, CO_2 and C_xH_y); 13 (CH^+ from C_xH_y); 14 (CH_2^+ and CO^{2+} from C_xH_y and CO; 15 (CH_3^+ from C_xH_y); 16 (O^+ and CH_4^+ from H_2O and CH_4); 17 (OH^+ from H_2O); 18 (H_2O^+ from H_2O); 22 (CO_2^{2+} from CO_2); 24 (C_2^+ from C_xH_y); 26 ($C_2H_2^+$ from C_xH_y); 27 ($C_2H_3^+$ from C_xH_y); 32 (O_2^+ from O_2); 35 ($^{35}Cl^+$ from Cl_2); 37 ($^{37}Cl^+$ from Cl_2); 38 ($H^{37}Cl^+$ from HCl and $C_3H_2^+$ from C_xH_y); 39 ($C_3H_3^+$ from C_xH_y); 41 ($C_3H_5^+$ from C_xH_y); 42 ($C_3H_6^+$ from C_xH_y); 43 ($C_3H_7^+$ from C_xH_y); 44 (CO_2^+ from CO_2); and 45 ($^{13}CO_2^+$ from CO_2).

[b]The agreement factor is defined as $R_w^2 = \frac{\sum(y_i^{obs} - y_i^{calc})^2}{\sum(y_i^{obs})^2} \times 100\%$, where y_i is the value at position *i*.

■ REFERENCES

(1) Ōya, A.; Marsh, H. Phenomena of Catalytic Graphitization. *J. Mater. Sci.* **1982**, *17*, 309−322.

(2) Ōya, A.; Ōtani, S. Catalytic Graphitization of Carbons by Various Metals. *Carbon* **1979**, *17*, 131−137.

(3) Homma, Y.; Kobayashi, Y.; Ogino, T.; Takagi, D.; Ito, R.; Jung, Y. J.; Ajayan, P. M. Role of Transition Metal Catalysts in Single-Walled Carbon Nanotube Growth in Chemical Vapor Deposition. *J. Phys. Chem. B* **2003**, *107*, 12161−12164.

(4) Wang, K.; Cao, Y.; Wang, X.; Kharel, P. R.; Gibbons, W.; Luo, B.; Gu, Z.; Fan, Q.; Metzger, L. Nickel Catalytic Graphitized Porous Carbon as Electrode Material for High Performance Supercapacitors. *Energy* **2016**, *101*, 9−15.

(5) Zhang, X.; Zhang, K.; Li, H.; Wang, Q.; Jin, L. e.; Cao, Q. Synthesis of Porous Graphitic Carbon from Biomass by One-Step Method And Its Role in the Electrode for Supercapacitor. *J. Appl. Electrochem.* **2018**, *48*, 415−426.

(6) Chang, B.; Guo, Y.; Li, Y.; Yin, H.; Zhang, S.; Yang, B.; Dong, X. Graphitized Hierarchical Porous Carbon Nanospheres: Simultaneous Activation/Graphitization and Superior Supercapacitance Performance. *J. Mater. Chem. A* **2015**, *3*, 9565−9577.

(7) Gomez-Martin, A.; Martinez-Fernandez, J.; Ruttert, M.; Heckmann, A.; Winter, M.; Placke, T.; Ramirez-Rico, J. Iron-Catalyzed Graphitic Carbon Materials from Biomass Resources as Anodes for Lithium-Ion Batteries. *ChemSusChem* **2018**, *11*, 2776−2787.

(8) Abdelwahab, A.; Castelo-Quibén, J.; Vivo-Vilches, J.; Pérez-Cadenas, M.; Maldonado-Hódar, F.; Carrasco-Marín, F.; Pérez-Cadenas, A. Electrodes Based on Carbon Aerogels Partially Graphitized by Doping with Transition Metals for Oxygen Reduction Reaction. *Nanomaterials* **2018**, *8*, 266.

(9) Chen, L.; Wang, H.; Wei, H.; Guo, Z.; Khan, M. A.; Young, D. P.; Zhu, J. Carbon Monolith with Embedded Mesopores and Nanoparticles as a Novel Adsorbent for Water Treatment. *RSC Adv.* **2015**, *5*, 42540−42547.

(10) Liu, Y.; Liu, Q.; Gu, J.; Kang, D.; Zhou, F.; Zhang, W.; Wu, Y.; Zhang, D. Highly Porous Graphitic Materials Prepared by Catalytic Graphitization. *Carbon* **2013**, *64*, 132−140.

(11) Popov, V. V.; Orlova, T. S.; Gutierrez-Pardo, A.; Ramirez-Rico, J. Features of Electrical Properties of BE-C(Fe) Biocarbons Carbonized in the Presence of an Fe-Containing Catalyst. *Phys. Solid State* **2017**, *59*, 703−709.

(12) Maldonado-Hódar, F. J.; Moreno-Castilla, C.; Rivera-Utrilla, J.; Hanzawa, Y.; Yamada, Y. Catalytic Graphitization of Carbon Aerogels by Transition Metals. *Langmuir* **2000**, *16*, 4367−4373.

(13) Yan, Q.; Li, J.; Zhang, X.; Hassan, E. B.; Wang, C.; Zhang, J.; Cai, Z. Catalytic Graphitization of Kraft Lignin to Graphene-Based Structures with Four Different Transitional Metals. *J. Nanoparticle Res.* **2018**, *20*, 223.

(14) Thambiliyagodage, C. J.; Ulrich, S.; Araujo, P. T.; Bakker, M. G. Catalytic Graphitization in Nanocast Carbon Monoliths by Iron, Cobalt and Nickel Nanoparticles. *Carbon* **2018**, *134*, 452−463.

(15) Sevilla, M.; Fuertes, A. B. Fabrication of Porous Carbon Monoliths with a Graphitic Framework. *Carbon* **2013**, *56*, 155−166.

(16) Sevilla, M.; Sanchís, C.; Valdés-Solís, T.; Morallón, E.; Fuertes, A. B. Synthesis of Graphitic Carbon Nanostructures from Sawdust and Their Application as Electrocatalyst Supports. *J. Phys. Chem. C* **2007**, *111*, 9749−9756.

(17) Sevilla, M.; Salinas Martínez-de Lecea, C.; Valdés-Solís, T.; Morallón, E.; Fuertes, A. B. Solid-Phase Synthesis of Graphitic Carbon Nanostructures from Iron and Cobalt Gluconates and Their Utilization as Electrocatalyst Supports. *Phys. Chem. Chem. Phys.* **2008**, *10*, 1433−1442.

(18) Wu, F.; Huang, R.; Mu, D.; Wu, B.; Chen, Y. Controlled synthesis of graphitic carbon-encapsulated α-Fe2O3 nanocomposite via low-temperature catalytic graphitization of biomass and its lithium storage property. *Electrochim. Acta* **2016**, *187*, 508−516.

(19) Zhou, H.-h.; Peng, Q.-l.; Huang, Z.-h.; Yu, Q.; Chen, J.-h.; Kuang, Y.-f. Catalytic Graphitization of PAN-Based Carbon Fibers with Electrodeposited Ni-Fe Alloy. *Trans. Nonferrous Met. Soc. China* **2011**, *21*, 581−587.

(20) Wang, J.; Deng, X.; Zhang, H.; Duan, H.; Cheng, F.; Zhang, S. Low-Temperature Catalytic Graphitization of Phenolic Resin Using a Co-Ni Bimetallic Catalyst. *Interceram* **2016**, *65*, 24−27.

(21) Gutiérrez-Pardo, A.; Ramírez-Rico, J.; Cabezas-Rodríguez, R.; Martínez-Fernández, J. Effect of Catalytic Graphitization on the Electrochemical Behavior of Wood Derived Carbons for Use in Supercapacitors. *J. Power Sources* **2015**, *278*, 18−26.

(22) Hoekstra, J.; Beale, A. M.; Soulimani, F.; Versluijs-Helder, M.; Geus, J. W.; Jenneskens, L. W. Base Metal Catalyzed Graphitization of Cellulose: A Combined Raman Spectroscopy, Temperature-Dependent X-Ray Diffraction and High-Resolution Transmission Electron Microscopy Study. *J. Phys. Chem. C* **2015**, *119*, 10653−10661.

(23) Thompson, E.; Danks, A. E.; Bourgeois, L.; Schnepp, Z. Iron-Catalyzed Graphitization of Biomass. *Green Chem.* **2015**, *17*, 551−556.

(24) Chen, L.; Ji, T.; Mu, L.; Shi, Y.; Brisbin, L.; Guo, Z.; Khan, M. A.; Young, D. P.; Zhu, J. Facile Synthesis of Mesoporous Carbon Nanocomposites from Natural Biomass for Efficient Dye Adsorption and Selective Heavy Metal Removal. *RSC Adv.* **2016**, *6*, 2259−2269.

(25) Ramirez-Rico, J.; Gutierrez-Pardo, A.; Martinez-Fernandez, J.; Popov, V. V.; Orlova, T. S. Thermal Conductivity of Fe Graphitized Wood Derived Carbon. *Mater. Des.* **2016**, *99*, 528−534.

(26) Kakunuri, M.; Kali, S.; Sharma, C. S. Catalytic Graphitization of Resorcinol-Formaldehyde Xerogel and Its Effect on Lithium Ion Intercalation. *J. Anal. Appl. Pyrolysis* **2016**, *117*, 317−324.
(27) Liu, S.; Loper, C. R. The Formation of Kish Graphite. *Carbon* **1991**, *29*, 547−555.
(28) Marsh, H.; Crawford, D.; Taylor, D. W. Catalytic Graphitization by Iron of Isotropic Carbon from Polyfurfuryl Alcohol, 725-1090 K. A High Resolution Electron Microscope Study. *Carbon* **1983**, *21*, 81−87.
(29) Krivoruchko, O. P.; Zaikovskii, V. I. A New Phenomenon Involving the Formation of Liquid Mobile Metal-Carbon Particles in the Low-Temperature Catalytic Graphitisation of Amorphous Carbon by Metallic Fe, Co and Ni. *Mendeleev Commun.* **1998**, *8*, 97−99.
(30) Glatzel, S.; Schnepp, Z.; Giordano, C. From Paper to Structured Carbon Electrodes by Inkjet Printing. *Angew. Chem., Int. Ed.* **2013**, *52*, 2355−2358.
(31) Feng, X.; Chee, S. W.; Sharma, R.; Liu, K.; Xie, X.; Li, Q.; Fan, S.; Jiang, K. In Situ TEM Observation of the Gasification and Growth of Carbon Nanotubes Using Iron Catalysts. *Nano Res.* **2011**, *4*, 767−779.
(32) Sevilla, M.; Fuertes, A. B. Catalytic Graphitization of Templated Mesoporous Carbons. *Carbon* **2006**, *44*, 468−474.
(33) Sevilla, M.; Sanchís, C.; Valdés-Solís, T.; Morallón, E.; Fuertes, A. B. Highly Dispersed Platinum Nanoparticles on Carbon Nanocoils and Their Electrocatalytic Performance for Fuel Cell Reactions. *Electrochim. Acta* **2009**, *54*, 2234−2238.
(34) Sevilla, M.; Fuertes, A. B. Graphitic Carbon Nanostructures from Cellulose. *Chem. Phys. Lett.* **2010**, *490*, 63−68.
(35) Gutiérrez-Pardo, A.; Ramírez-Rico, J.; de Arellano-López, A. R.; Martínez-Fernández, J. Characterization of Porous Graphitic Monoliths from Pyrolyzed Wood. *J. Mater. Sci.* **2014**, *49*, 7688−7696.
(36) Yudasaka, M.; Tasaka, K.; Kikuchi, R.; Ohki, Y.; Yoshimura, S.; Ota, E. Influence of Chemical Bond of Carbon on Ni Catalyzed Graphitization. *J. Appl. Phys.* **1997**, *81*, 7623−7629.
(37) Juhás, P.; Davis, T.; Farrow, C. L.; Billinge, S. J. L. PDFgetX3: A Rapid and Highly Automatable Program for Processing Powder Diffraction Data into Total Scattering Pair Distribution Functions. *J. Appl. Crystallogr.* **2013**, *46*, 560−566.
(38) Farrow, C. L.; Juhas, P.; Liu, J. W.; Bryndin, D.; Božin, E. S.; Bloch, J.; Proffen, T.; Billinge, S. J. L. PDFfit2 and PDFgui: Computer Programs for Studying Nanostructure in Crystals. *J. Phys. Condens. Matter* **2007**, *19*, 335219.
(39) Yang, H.; Yan, R.; Chen, H.; Lee, D. H.; Zheng, C. Characteristics of Hemicellulose, Cellulose and Lignin Pyrolysis. *Fuel* **2007**, *86*, 1781−1788.
(40) Aravind, S. S. J.; Eswaraiah, V.; Ramaprabhu, S. Facile and Simultaneous Production of Metal/Metal Oxide Dispersed Graphene Nano Composites by Solar Exfoliation. *J. Mater. Chem.* **2011**, *21*, 17094−17097.
(41) Zhu, X.; Qian, F.; Liu, Y.; Matera, D.; Wu, G.; Zhang, S.; Chen, J. Controllable Synthesis of Magnetic Carbon Composites with High Porosity and Strong Acid Resistance from Hydrochar for Efficient Removal of Organic Pollutants: An Overlooked Influence. *Carbon* **2016**, *99*, 338−347.
(42) Kanungo, S. B.; Mishra, S. K. Thermal dehydration and decomposition of FeCl3·xH2O. *J. Therm. Anal.* **1996**, *46*, 1487−1500.
(43) Cazetta, A. L.; Pezoti, O.; Bedin, K. C.; Silva, T. L.; Paesano Junior, A.; Asefa, T.; Almeida, V. C. Magnetic Activated Carbon Derived from Biomass Waste by Concurrent Synthesis: Efficient Adsorbent for Toxic Dyes. *ACS Sustain. Chem. Eng.* **2016**, *4*, 1058−1068.
(44) Wiberg, N.; Holleman, A. F.; Wiberg, E. *Inorganic Chemistry*; Academic Press, 2001; pp 1430−1457.
(45) Deck, C. P.; Vecchio, K. Prediction of Carbon Nanotube Growth Success by the Analysis of Carbon-Catalyst Binary Phase Diagrams. *Carbon* **2006**, *44*, 267−275.
(46) Billinge, S. J. L.; Kanatzidis, M. G. Beyond Crystallography: The Study of Disorder, Nanocrystallinity and Crystallographically Challenged Materials with Pair Distribution Functions. *Chem. Commun.* **2004**, 749−760.
(47) Franklin, R. E. Crystallite Growth in Graphitizing and Non-Graphitizing Carbons. *Proc. R. Soc. London, Ser. A* **1951**, *209*, 196−218.
(48) Franklin, R. E. The Interpretation of Diffuse X-Ray Diagrams of Carbon. *Acta Crystallogr.* **1950**, *3*, 107−121.
(49) Petkov, V.; Difrancesco, R. G.; Billinge, S. J. L.; Acharya, M.; Foley, H. C. Local Structure of Nanoporous Carbons. *Philos. Mag. B* **1999**, *79*, 1519−1530.
(50) Gomez-Martin, A.; Martinez-Fernandez, J.; Ruttert, M.; Winter, M.; Placke, T.; Ramirez-Rico, J. Correlation of Structure and Performance of Hard Carbons as Anodes for Sodium Ion Batteries. *Chem. Mater.* **2019**, *31*, 7288−7299.
(51) Petkov, V.; Trikalitis, P. N.; Bozin, E. S.; Billinge, S. J. L.; Vogt, T.; Kanatzidis, M. G. Structure of V2O5·nH2O Xerogel Solved by the Atomic Pair Distribution Function Technique. *J. Am. Chem. Soc.* **2002**, *124*, 10157−10162.
(52) Egami, T.; Billinge, S. J. L. Extracting Structural Information from the PDF. *Underneath the Bragg Peaks, Structural Analysis of Complex Materials*; Egami, T., Billinge, S. J. L., Eds.; Pergamon, 2003; pp 219−245.
(53) Stratford, J. M.; Allan, P. K.; Pecher, O.; Chater, P. A.; Grey, C. P. Mechanistic Insights into Sodium Storage in Hard Carbon Anodes Using Local Structure Probes. *Chem. Commun.* **2016**, *52*, 12430−12433.
(54) Liu, L.; Sun, J.; Li, M.; Wang, S.; Pei, H.; Zhang, J. Enhanced enzymatic hydrolysis and structural features of corn stover by FeCl3 pretreatment. *Bioresour. Technol.* **2009**, *100*, 5853−5858.
(55) Li, J.; Zhang, X.; Zhang, M.; Xiu, H.; He, H. Optimization of Selective Acid Hydrolysis of Cellulose for Microcrystalline Cellulose using FeCl3. *BioResources* **2014**, *9*, 1334.
(56) Karim, M.; Chowdhury, Z.; Hamid, S.; Ali, M. Statistical Optimization for Acid Hydrolysis of Microcrystalline Cellulose and Its Physiochemical Characterization by Using Metal Ion Catalyst. *Materials* **2014**, *7*, 6982−6999.
(57) Inagaki, M.; Kang, F. Fundamental Science of Carbon Materials. *Materials Science and Engineering of Carbon: Fundamentals*; Elsevier, 2014; pp 17−217.
(58) Lian, W.; Song, H.; Chen, X.; Li, L.; Huo, J.; Zhao, M.; Wang, G. The transformation of acetylene black into onion-like hollow carbon nanoparticles at 1000°C using an iron catalyst. *Carbon* **2008**, *46*, 525−530.
(59) Neeli, S. T.; Ramsurn, H. Synthesis and formation mechanism of iron nanoparticles in graphitized carbon matrices using biochar from biomass model compounds as a support. *Carbon* **2018**, *134*, 480−490.
(60) Ōya, A.; Ōtani, S. Influences of Particle Size of Metal on Catalytic Graphitization of Non-Graphitizing Carbons. *Carbon* **1981**, *19*, 391−400.
(61) Bale, C. W.; Bélisle, E.; Chartrand, P.; Decterov, S. A.; Eriksson, G.; Hack, K.; Jung, I.-H.; Kang, Y.-B.; Melançon, J.; Pelton, A. D.; Robelin, C.; Petersen, S. FactSage Thermochemical Software and Databases - Recent Developments. *CALPHAD: Comput. Coupling Phase Diagrams Thermochem.* **2009**, *33*, 295−311.
(62) Mattevi, C.; Kim, H.; Chhowalla, M. A Review of Chemical Vapour Deposition of Graphene on Copper. *J. Mater. Chem.* **2011**, *21*, 3324−3334.
(63) Li, H.; Zhang, H.; Li, K.; Zhang, J.; Sun, M.; Su, B. Catalytic Graphitization of Coke Carbon by Iron: Understanding the Evolution of Carbon Structure, Morphology and Lattice Fringes. *Fuel* **2020**, *279*, 118531.

https://doi.org/10.1021/acs.chemmater.0c04385
Chem. Mater. 2021, 33, 3087−3097